Observations of 4.26μm CO_2 Auroral Emissions from AIRS Nadir Sounder Measurements

Katrina Bossert[1,2], Lars Hoffmann[3], Martin Mlynczak[4], and Linda Hunt[5]

[1]School of Earth and Space Exploration, Arizona State University, Tempe, AZ, USA

[2]School of Mathematical and Statistical Sciences, Arizona State Univeristy, Tempe, AZ, USA

[3] Jülich Supercomputing Centre, Forschungszentrum Jülich, Jülich, Germany

[4]NASA Langley Resesarch Center, Hampton, VA, USA

[5]Science Systems and Applications, Inc., Hampton, VA, USA

Corresponding author: Katrina Bossert (katrina.bossert@asu.edu)

Key Points:

- A carbon dioxide infrared emission at 4.26 microns associated with the aurora is observed by the AIRS instrument
- A new non-local thermodynamic equilibrium (NLTE) index provides a quantitative measure of the carbon dioxide auroral-associated emission
- The AIRS auroral observations are confirmed by simultaneous SABER measurements and the SuperMAG Electrojet index

Abstract

The Atmospheric Infrared Sounder (AIRS) instrument onboard the NASA Aqua satellite is used to observe aurora associated with the CO_2 4.26 μm emission. These observations are due to non-local thermodynamic equilibrium (NLTE) resulting from the vibrational excitation of CO_2, which arises in the process of auroral energetic particle precipitation, as opposed to the dayside NLTE occurring due to solar radiation. The observations are confirmed to be associated with aurora using the Sounding of the Atmosphere using Broadband Emission Radiometry (SABER) limb measurements and the SuperMAG Electrojet (SME) index. The high spectral resolution and low noise associated with the AIRS instrument allows for the emission spectrum to be calculated and confirmed to arise from CO_2. Our new NLTE index values derived from AIRS provide the ability to globally measure auroral events associated with CO_2 with a spatial resolution on the order of ~13.5 km.

Plain Language Summary

The aurora are caused by energetic particle precipitation into Earth's atmosphere due to energy buildup and release in Earth's magnetic field from interaction with the solar wind. These energetic particles smash into Earth's atmosphere with high energy, and react with atoms and molecules in the atmosphere. There are many types of emissions of light that are associated with Earth's aurora. One of these emissions is the infrared emission centered near 4.26μm associated with excited CO_2 molecules. When CO_2 is vibrationally excited through an exchange of energy with an N_2 molecule excited by auroral particles, the CO_2 molecule eventually relaxes from this state and releases a photon near 4.26 μm. This research presents a satellite observation from NASA's AIRS instrument allowing for the CO_2 auroral emission to be viewed and mapped from space.

1 Introduction

The Atmospheric Infrared Sounder (AIRS) instrument onboard the NASA Aqua satellite was launched in 2002 and has been used to study the temperature in the stratosphere using CO_2 emissions at 4.26 μm and 15 μm [Hoffmann and Alexander, 2009]. While both of these emissions can be used to study temperatures during thermodynamic equilibrium, the 4.26 μm emission specifically is more sensitive non-local thermodynamic equilibrium (NLTE) during the daytime [DeSouza-Machado et al., 2007]. For a nadir sounder such as AIRS, the 4.3 μm NLTE effect can be measured, while the 15 μm NLTE effect is too small to be observed. Additionally, the 4.26 μm emission itself is susceptible to enhancements due to energetic particle precipitation during geomagnetic disturbances. This emission enhancement is known for both NO^+ [Mertens et al., 2008a; Mertens et al., 2008b; O'Neil et al., 2007] and CO_2 [Winick et al., 1987; Kumer, 1977; Sharma et al., 2015; Kalogerakis et al., 2016]. The CO_2 auroral excitation results in NLTE, and has previously been discussed with regards to the Cross-track Infrared Sounder (CrIS) NLTE observations in comparison to modeled NLTE radiances, which do not capture the full contribution to NLTE due to aurora [Li et al., 2020], as models have assumed NLTE conditions that occur during the daytime. Additionally, broadband IR measurements from VIIRS have also detected auroral emissions [Seaman and Miller, 2013], and the range of observed infrared wavelengths includes the NO^+ and CO_2 emissions.

Energetic particle precipitation changes the thermal energy balance in the mesosphere, thermosphere, and ionosphere. It results in significant chemical reactions, making energetic particle precipitation of interest for understanding both the chemistry and thermodynamics in this region of the atmosphere. Satellite and ground-based imaging of specific emission lines associated with aurora have been used to calculate auroral input energy to energetic particle precipitation [Gabrielse et al., 2021; Li et al., 2022; Hecht et al., 1989; Hecht et al., 2006; Strickland et al., 1989; Sotirelis et al., 2013]. Energetic particle precipitation from aurora and solar activity has also been associated with increased NOx [Randall et al., 2007; Lopez-Puertas et al., 2005]. The necessity of understanding the full spectrum of energetic electrons for adequately characterizing the chemistry in the middle atmosphere has also previously been discussed [Randall et al., 2015]. Additionally, understanding energetic input due to aurora and particle precipitation is important for linking to atmospheric dynamics such as the generation of traveling ionospheric disturbances due to joule heating [Sheng et al., 2020].

Observations presented here demonstrate an AIRS 4.26 μm emission associated with auroral precipitation. The observations are compared with SABER observations and the SME. These AIRS measurements provide a unique means of observing auroral emissions at 4.26 μm spatially with a nadir viewing instrument. The emission spectra from the nadir measurements in this spectral range were found to be largely due to CO_2. To isolate emissions due to 4.26 μm, a new NLTE index, discussed in the following sections, is calculated. The results provide a map of CO_2 emissions during nighttime conditions due to energetic particle precipitation from aurora.

2 Data and Methods

2.1 The AIRS instrument and a measurement derived NLTE index

In this study, we initially identified the presence of NLTE effects in the AIRS observations by visual inspection of radiance measurements covering the 4.26 and 15 μm carbon dioxide (CO_2) fundamental bands. As an example, Fig. 1 shows spectral mean radiances of granule 32 of AIRS measurements on 14 October 2016, measured from 3:12-3:18 UTC using a set of 75 channels from 2310 cm^{-1} to 2380 cm^{-1} covering the 4.26 μm waveband and a set of 120 channels from 650 cm^{-1} to 680 cm^{-1} covering the 15 μm waveband. Here, the radiance measurements of the two channel set have been averaged to reduce the measurement noise and to make some weaker NLTE features visible. A visual inspection of the AIRS nighttime measurements shows locally increased radiances due to NLTE in the 4.26 μm waveband (Fig. 1a), which are absent in the 15 μm waveband (Fig. 1b). The increased 4.26 μm radiances are found in a belt extending from Iceland to Scandinavia from 65 to 70°N. The belt of increased radiances is co-located with the Aurora Borealis and attributed to excitation of the CO_2 molecules to NLTE conditions, which will be shown and further discussed in following sections.

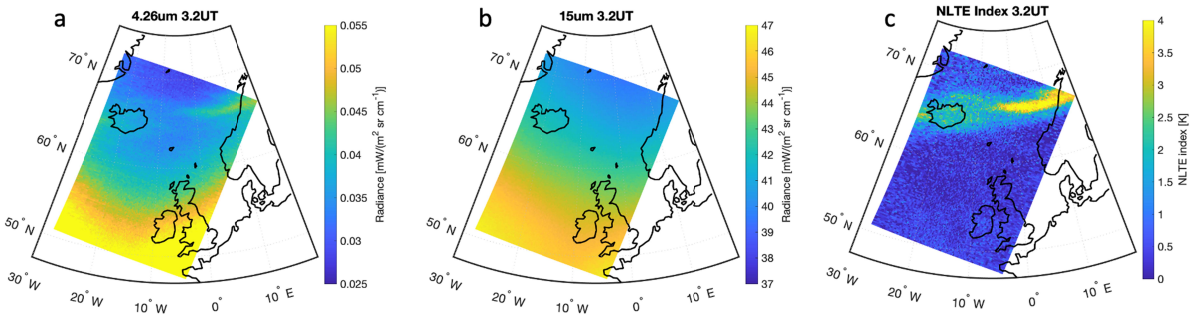

Figure 1: An example AIRS granule is used at ~3.2UT on 14 October 2016 to demonstrate average spectral radiances associated with aurora. Plot a shows spectral radiances averaged over 75 channels from 2310 cm^{-1} to 2380 cm^{-1} covering the 4.26 µm emission. Plot b shows spectral radiances averaged over 120 channels from 650 cm^{-1} to 680 cm^{-1} covering the 15 µm waveband. Plot c shows the calculated NLTE index.

In order to quantify the strength of the NLTE signals in the AIRS measurements, we defined a NLTE index (NI) using the 4.26 and 15 micron radiance measurements. Such an NI can be defined in various ways. In principle, it could be defined as simple as taking a brightness temperature difference of the 4.26 and 15 µm radiance measurements of each satellite footprint. However, we found this approach did not work well because the 4.26 and 15 µm AIRS channel sets considered here have different spectral mean vertical coverage and sensitivity due to the different temperature weighting functions, which would map into the calculation of the NI. Next to spectral differencing for defining the NI, another option would be spatial differencing of radiance measurements using separate footprints located inside or outside regions being affected by NLTE. However, spatial differencing requires various choices and parameter tests of the method, e. g., with respect to proper smoothing and removal of the background-state. For these reasons, we developed a more sophisticated approach to define and calculate an NI from the AIRS measurements.

We calculate the NI from the AIRS measurements in a two-step procedure. In the first step, we conduct a full non-linear stratospheric temperature retrieval using the AIRS measurements in the 15 µm waveband. The retrieval scheme applied here is essentially the same as the retrieval scheme described by Hoffmann and Alexander (2009). The retrieval provides stratospheric temperatures in the height range of about 20 to 55 km with a vertical resolution of 7 to 11 km and retrieval noise of about 1.5 to 2K in the same range. While the retrieval applies a radiative transfer model that is not capable of simulating NLTE effects, the retrieved temperature profile $\hat{T}_{\mathrm{LTE}}(z,15\mu m)$ is not affected by this, because the 15 µm channels applied in the scheme are not affected by NLTE [de Souza-Machado et al., 2006]. In the second step, we apply the radiative transfer model and the temperature profile retrieved from the 15 µm radiance measurements to simulate the 4.26 µm radiance measurements AIRS would make under LTE conditions. Finally, the NI is calculated as the difference between the real AIRS spectral mean brightness temperature measurements including the NLTE effects and the simulated brightness temperature measurements assuming LTE conditions,

$$NI = \overline{BT}_{meas}\left(4.26\mu m, T_{non-LTE}(z)\right) - \overline{BT}_{sim}\left(4.26\mu m, \hat{T}_{LTE}(z, 15\mu m)\right) \quad (1)$$

As an example, Fig. 1c shows the NI calculated from the AIRS measurements for the case study discussed earlier. As NLTE conditions yield increased molecular excitation and increased radiance emitted by the CO_2 molecules, the NI increases in the presence of NLTE conditions. From the example shown here, the maximum NI is about 4K whereas the measurement noise is about 0.5 K. We note that while the NI is usually well-defined, in the case of extreme temperature fluctuations, e.g., due to the presence of large-amplitude mountain waves, the index may misdetect these fluctuations as NLTE signals. This issue arises from remaining, small differences in terms of vertical coverage and sensitivity of the AIRS 4.26 and 15 μm channels selected for this analysis. However, based on the inspection of a larger number of cases of AIRS NLTE observations, we conclude that this issue is generally not severe, but should be kept in mind when analysing individual cases. Such cases can be identified using gravity wave detection methods for AIRS observations as described by Hoffmann et al. (2013, 2014).

2.2 Comparison of AIRS NLTE index and SME data

The NLTE index was calculated over the northern polar region for a time period of increased auroral activity. The time period extends from 7.5UT on 13 October 2016 to 6.5 UT on 14 October 2016 and uses 15 granules. The resulting NLTE index signals in Fig. 2a clearly show the shape of the aurora. AIRS nightside granules were used (solar zenith angles were between 100-130 degrees for data shown), and these times approximately spanned just before magnetic midnight to a few hours before magnetic midnight, which generally overlaps times of expected auroral activity on the night side (Laundal and Richmond, 2016). While not shown here, similar emissions can be observed in the southern hemisphere during nighttime conditions. The SuperMAG Electrojet (SME) index [Newell and Gjerloev, 2011a, 2011b; Gjerloev, 2012] is associated with global auroral power. The SME uses over 100 magnetometer sites as opposed to the 12 used in the auroral electrojet (AE) index calculation, and has previously demonstrated a strong correlation with total nightside auroral power. The SME is used here to demonstrate times of increased auroral activity.The SME is plotted during an overlapped time range in Fig. 2b. As can be observed from the plots in Fig 2, the times of stronger NLTE index signals correspond to times of stronger SME index. This comparison provides a means of demonstrating the auroral influence on AIRS NLTE index calculations. Fig 2a also shows how this data product can be used to give a global snapshot of hemispheric auroral activity over a 24 hour period.

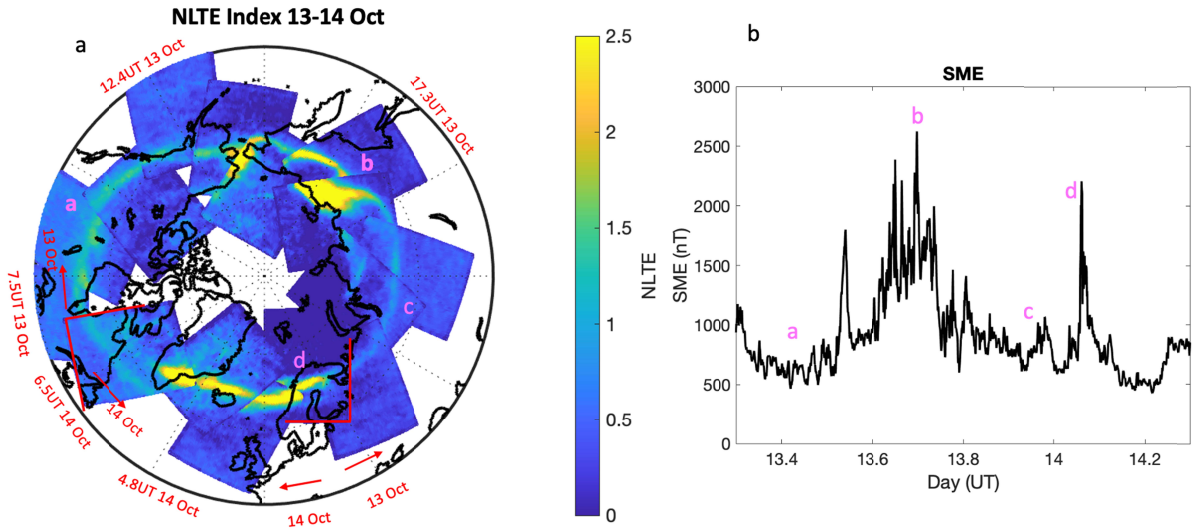

Figure 2: Plot a shows the AIRS NLTE Index calculated for 15 granules over a 24 hour period of increased auroral activity. Plot b shows the SME index for the same time period demonstrating that times of increased SME correspond to increased NLTE Index.

2.3 Comparison with SABER coincident measurements

The AIRS NLTE index observations were further compared to coincident SABER measurements to verify the presence of auroral emissions. Fig. 3a shows an AIRS granule 15 (1:30-1:36UT) with calculated NLTE index values on 14 October 2016. Figs 3b-d show coincident SABER spectrally integrated radiance measurements of CO_2 15.2 µm, CO_2 4.26 µm, and O_2 1.28 µm VER during this time. Fig. 3e shows AIRS granule 32 (3:12-3:18UT) and corresponding NLTE index signals on 14 October 2016. Corresponding SABER measurements are shown in Figs. 3f-h. In both cases, SABER demonstrates there is no enhancement in 15.2 µm overlapping the regions closest to the largest AIRS NLTE index calculation. SABER has previously been used to demonstrate an auroral enhancement in the 4.26 µm channel due to CO_2 [Winick et al., 2004], and at higher altitudes due to NO^+ [Mertens et al., 2008a; Mertens et al., 2008b]. Enhancements in the SABER 4.26 µm channel are observed for these AIRS overlap examples, especially for the limb views that most closely overlap the aurora (red dots in Figs. a and e, and red lines in Figs. c and g). SABER has also been used to study auroral emissions associated with O_2 airglow at 1.28 µm [Gao et al., 2020]. For these cases, enhancements are observed in the 1.28 µm channel from ~100-120km. It is noted here that SABER measurements are limb measurements, so have more sensitivity to emissions at higher altitudes associated with NO^+ [Mertens et al, 2008b], that would otherwise be weak compared to emissions from CO_2 viewed from the nadir, as is the case with the AIRS measurements. Also, SABER does not have the spectral resolution to differentiate those 4.26 µm emissions that occur from CO_2 versus NO^+. SABER measurements are shown here to validate that the increased AIRS NLTE index signals overlap regions of auroral

emissions. These measurements confirm the presence of aurora and increased 4.26 µm emission in SABER where AIRS measurements show increased NLTE index calculations.

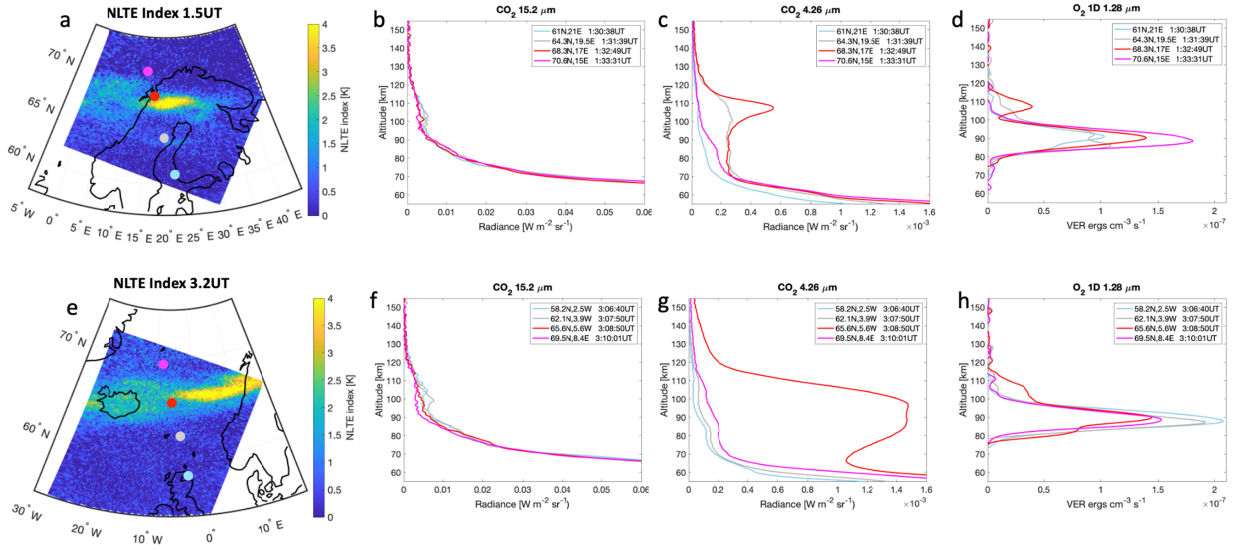

Figure 3: Plot a shows the AIRS NLTE index on 14 October 2016 at 1.5UT. Plots b-d show corresponding SABER plots closely overlapping the AIRS observation in both time and spatial extent. Plots e-h show the same for observations at 3.2UT. The dots in plot a and e show the SABER location of the measurement, and the colors correspond to those used in plots b-d and f-h.

3 Discussion: The CO_2 auroral emission

The AIRS instrument can detect emissions in the range of the CO_2 4.26 µm (2347 cm^{-1}) waveband with a spectral resolution of ~1 cm^{-1}. Given this precision, the emissions outside of the region of NLTE index enhancement due to aurora can be subtracted from the region of enhanced NLTE emission to retrieve a spectral differencing at each wavenumber measured by AIRS, resulting in an emission spectrum associated with auroral emissions. Fig. 4 shows an example of this process. Figure 4a shows the NLTE index granule to be used, in this case the event on 14 October at 3.2UT. Figure 4b shows the regions of low NI with values < 0.3 in blue, and regions of high NLTE index with values > 1.8 in red. In order to remove background emission signal and be left with perturbations solely due to the auroral emission, a fourth order polynomial was fit along each zonal direction of the granule for each emission channel, and the resulting fit was subtracted. It is noted that this was applied to a granule with no small-scale temperature fluctuations (e.g. gravity waves) that would cause significant variations in CO_2 emission intensity over the area of the granuale. Since this subtraction results in the auroral region itself appearing as a perturbation, the absolute value of the residual signal was used for each channel to compare regions of high and low NI. The average of the absolute value residual radiances in the low NLTE index region is subtracted from the average of the absolute value residual radiances in the high NLTE index region for each observed frequency from 2266 cm^{-1} to 2383 cm^{-1}. Due to degradation, some channels were removed based on quality indicators within the Level-1B data

files. Channels 1985, 2053, and 2075, or 2295.7 cm^{-1}, 2334.7 cm^{-1}, and 2355.4 cm^{-1} were removed. A total of 118 frequency channels were used in the differencing. The mean of the residual spectral radiance values for NLTE index > 1.8 and NLTE index < 0.3 are shown in Fig 3c. The resulting mean difference for each channel is shown in Fig. 4d.

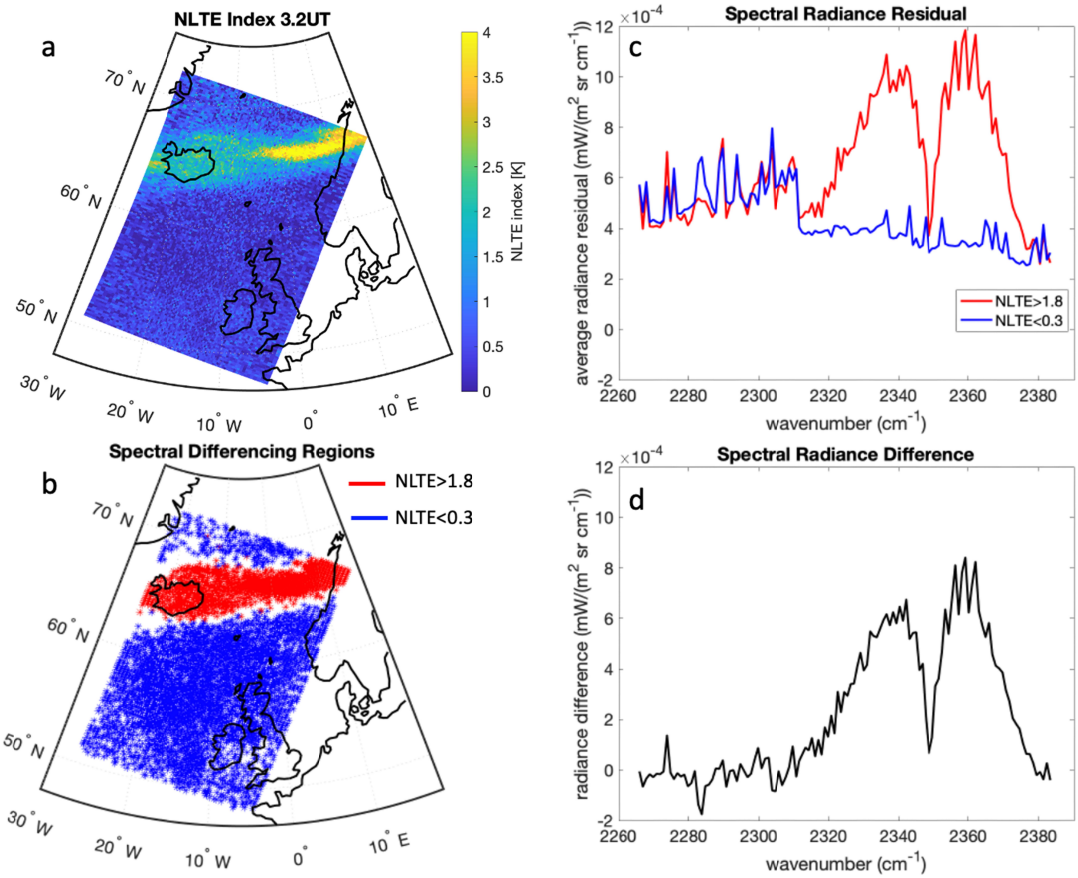

Figure 4: Plot a shows the NLTE index values at 3.2 UT on 14 October 2016. Plot b shows the masked NLTE index value regions with values < 0.3 in blue, and regions of high NLTE index with values > 1.8 in red. Plot c shows the average residual spectral radiance values for the high and low NI regions. Plot d shows the spectral radiance difference between the high NI and low NI regions.

From the data presented in Fig. 4d, the emission is centered at 2347 cm^{-1}, and is no longer observed at wavenumbers less than 2300 cm^{-1}, which would be expected for the CO_2 associated auroral emission. The spectral shape closely matches the spectral shape (P,R branch) of the 4.26 micron CO_2 waveband. This indicates that the AIRS observations are largely from the CO_2 4.26 µm emission associated with the aurora. Although NO^+ auroral emissions are also expected, they would occur with a much weaker emission and are likely below the noise threshold of detection of AIRS. The CO_2 auroral emission has previously been discussed [Kumer, 1977; Winick et al., 2004; Kalogerakis et al., 2016; Sharma et al., 2015] and occurs due to vibrational excitation of CO_2 due to a collision with a vibrationally excited N_2 molecule, and subsequent relaxation with emission near 4.26 µm. While the study discussed here specifically focuses on

aurora observed during nighttime conditions during strong geomagnetic activity, it is noted that this result would also be expected to occur during any energetic particle precipitation or process that causes a vibrationally excited state of N_2. This includes aurora occurring on the dayside, which has not been investigated with the technique presented here.

4 Summary

We have demonstrated that hyperspectral nadir infrared sounders such as AIRS can observe the CO_2 emissions associated with aurora during nighttime conditions. The AIRS instrument has the spectral resolution to demonstrate that these emissions arise from the CO_2 emission centered at 4.26 μm. The observations are confirmed to overlap aurora through the use of near-coincident SABER measurements and the SME index data. These are the first nadir satellite observations of confirmed CO_2 auroral emission. The method presented here highlights a new dataset using the derived non-local thermodynamic equilibrium index, which can be used for the study of aurora and associated CO_2 excitation. This method uses AIRS granules, allowing for a spatial view of the auroral emission, and also providing a map view spanning the auroral oval.

Acknowledgments

KB acknowledges support from NASA 80NSSC21K0002. MM and LH acknowledge support from the NASA Heliophysics TIMED Project that supports the SABER Instrument Team. We gratefully acknowledge the SuperMAG collaborators for the use of the SME index.

Open Research

All datasets used in this work are publicly available.
AIRS calculated NLTE values (Hoffmann et al., 2023) are available at: https://datapub.fz-juelich.de/slcs/airs/nlte/
SABER data are available at: https://saber.gats-inc.com/data.php
SME data are available at: https://supermag.jhuapl.edu/indices

References

DeSouza-Machado, S. G., L. L. Strow, S. E. Hannon, H. E. Motteler, M. Lopez-Puertas, B. Funke, D. P. Edwards (2007), Fast forward radiative transfer modeling of 4.3 mm nonlocal thermodynamic equilibrium effects for infrared temperature sounders, Geophys. Res. Lett., 34, L01802, doi:10.1029/2006GL026684.

Gabrielse C, Nishimura T, Chen M, Hecht JH, Kaeppler SR, Gillies DM, Reimer AS, Lyons LR, Deng Y, Donovan E and Evans J (2021) Estimating Precipitating Energy Flux, Average Energy, and Hall Auroral Conductance From THEMIS All-Sky-Imagers With Focus on Mesoscales. Front. Phys. 9:744298. doi:10.3389/fphy.2021.744298.

Gao, H., Xu, J., Chen, G.-M., Zhu, Y., Liu, W., and Wang, C. (2020). Statistical structure of nighttime O2 aurora from SABER and its dependence on geomagnetic and solar activities in

284 winter. Journal of Geophysical Research: Space Physics, 125, e2020JA028302.
285 https://doi.org/10.1029/2020JA028302
286
287 Gjerloev, J. W. (2012), The SuperMAG data processing technique, J. Geophys. Res., 117,
288 A09213, doi:10.1029/2012JA017683.
289
290 Hecht JH, Christensen AB, Strickland DJ, and Meier RR. Deducing Composition and Incident
291 Electron Spectra from Ground-Based Auroral Optical Measurements: Variations in Oxygen
292 Density. J Geophys Res (1989) 94:13553–13563. doi:10.1029/JA094iA10p13553.
293
294 Hecht JH, Strickland DJ, and Conde MG. The Application of Ground-Based Optical Techniques
295 for Inferring Electron Energy Deposition and Composition Change during Auroral Precipitation
296 Events. J Atmos Solar-Terrestrial Phys (2006) 68(13):1502–19. doi:10.1016/j.jastp.2005.06.022
297
298 Hoffmann, Lars, 2023, "AIRS/Aqua Observations of non-LTE
299 Emissions", https://doi.org/10.26165/JUELICH-DATA/PHL4EE, Jülich DATA, V1
300
301 Hoffmann, L., and M. J. Alexander (2009), Retrieval of stratospheric temperatures from
302 Atmospheric Infrared Sounder radiance measurements for gravity wave studies, J. Geophys.
303 Res., 114, D07105, doi:10.1029/2008JD011241.
304
305 Hoffmann, L., X. Xue, and M. J. Alexander (2013), A global view of stratospheric gravity wave
306 hotspots located withAtmospheric Infrared Sounder observations, J. Geophys. Res. Atmos., 118,
307 416–434, doi:10.1029/2012JD018658.
308
309 Hoffmann, L., M. J. Alexander, C. Clerbaus, A. W. Grimsdell, C. I. Meyer, T. Rossler, and B.
310 Tournier (2014), Intercomparison of stratospheric gravity wave observations with AIRS and
311 IASI, Atmos. Meas. Tech., 7, 4517-4537, doi:10.5194/amt-7-4517-2014.
312
313 Kalogerakis, K. S., D. Matsiev, R. D. Sharma, and P. P. Wintersteiner (2016), Resolving the
314 mesospheric nighttime 4.3 μm emission puzzle: Laboratory demonstration of new mechanism for
315 OH(υ) relaxation, Geophys. Res. Lett., 43, doi:10.1002/2016GL069645.
316
317 Kumer, J. B. (1977), Theory of the CO2 4.3-micrometer Aurora and Reltated Phenomena, J.
318 Geophys. Res., Vol. 82, No. 16, 2203-2209.
319
320 Laundel, K. M., and A. D. Richmond (2016), Magnetic Coordinate Systems, Space Sci. Rev.,
321 DOI: 10.1007/s11214-016-0275-y.
322
323 Li, J., Matsuo, T., & Kilcommons, L.M. (2022). Assimilative mapping of auroral electron energy
324 flux using SSUSI Lyman-Birge-Hopfield (LBH) emissions. Journal of Geophysical Research:
325 Space Physics, 127, e2021JA029739. https://doi.org/10.1029/2021JA029739
326
327 Li, Z., Menzel, W. P., Jung, J., Lim, A., Li, J., Matricardi, M., et al. (2020). Improving the
328 understanding of CrIS full spectral resolution nonlocal thermodynamic equilibrium radiances

using spectral correlation. Journal of Geophysical Research: Atmospheres, 125, e2020JD032710. https://doi.org/10.1029/2020JD032710

López-Puertas, M., Funke, B., Gil-López, S., von Clarmann, T., Stiller, G. P., Höpfner, M., Kellmann, S., Fischer, H., and Jackman, C. H. (2005), Observation of NO_x enhancement and ozone depletion in the Northern and Southern Hemispheres after the October–November 2003 solar proton events, *J. Geophys. Res.*, 110, A09S43, doi:10.1029/2005JA011050.

Mertens, C. J., J. R. Fernandez, X. Xu, D. S. Evans, M. G. Mlynczak, J. M. Russell III (2008a), A new source of auroral infrared emission observed by TIMED/SABER, Geophys. Res. Lett., Vol. 35, L17106, doi:10.1029/2008GL034701.

Mertens, C. J., J. R. Winick, R. H. Picard, D. S. Evans, M. Lopez-Puertas, P. P. Wintersteiner, X. Xu, M. G. Mlynczak, J. M. Russell III (2008b), Influence of solar-geomagnetic disturbances on SABER measurements of 4.3 um emission and the retrieval of kinetic temperature and carbon dioxide, Adv. Space Res., 43, 1325-1336.

Newell, P.T., & Gjerloev, J. W. (2011a). Evaluation of SuperMAG auroral electrojet indices as indicators of substorms and auroral power. Journal of Geophysical Research, 116, A12211. https://doi.org/10.1029/2011JA016779

Newell, P.T., & Gjerloev, J. W. (2011b). Substorm and magnetosphere characteristic scales inferred from the SuperMAG auroral electrojet indices. Journal of Geophysical Research, 116, 12232. https://doi.org/10.1029/2011JA016936

O'Neil, R. R., J. R. Winick, R. H. Picard, and M. Kendra (2007), Auroral NO+ 4.3 mm emission observed from the Midcourse Space Experiment: Multiplatform observations of 9 February 1997, J. Geophys. Res., 112, A06327, doi:10.1029/2006JA012120.

Randall, C. E., V. L. Harvey, L. A. Holt, D. R. Marsh, D. Kinnison, B. Funke, and P. F. Bernath (2015), Simulation of energetic particle precipitation effects during the 2003–2004 Arctic winter, J. Geophys. Res. Space Physics, 120, 5035–5048, doi:10.1002/2015JA021196.

Randall, C. E., V. L. Harvey, C. S. Singleton, S. M. Bailey, P. F. Bernath, M. Codrescu, H. Nakajima, and J. M. Russell III (2007), Energetic particle precipitation effects on the Southern Hemisphere stratosphere in 1992–2005, J. Geophys. Res., 112, D08308, doi:10.1029/2006JD007696.

Seaman, C. J., & Miller, S. D. (2013). VIIRS captures aurora motions. Bulletin of the American Meteorological Society, 94(10), 1491–1493. https://doi.org/10.1175/BAMS-D-12-00221.1

Sharma, R. D., P. P. Wintersteiner, and K. S. Kalogerakis (2015), A new mechanism for OH vibrational relaxation leading to enhanced CO2 emissions in the nocturnal atmosphere, Geophys. Res. Lett., 42, 4639–4647, doi:10.1002/2015GL063724.

374 Sheng, C., Deng, Y., Zhang, S.-R., Nishimura, Y., & Lyons, L. R. (2020). Relative contributions
375 of ion convection and particle precipitation to exciting large-scale traveling atmospheric and
376 ionospheric disturbances. Journal of Geophysical Research: Space Physics, 125,
377 e2019JA027342. https://doi.org/10.1029/2019JA027342
378
379 Sotirelis, T., H. Korth, S.-Y. Hsieh, Y. Zhang, D. Morrison and L. Paxton (2013), Empirical
380 relationship between electron precipitation and far-ultraviolet auroral emissions from DMSP
381 observations, J. Geophys. Res. Space Physics, 118, 1203–1209, doi:10.1002/jgra.50157.
382
383 Strickland DJ, Meier RR, Hecht JH, and Christensen AB. Deducing Composition and Incident
384 Electron Spectra from Ground-Based Auroral Optical Measurements: Theory and Model Results.
385 J Geophys Res (1989) 94(13):13527–13539. doi:10.1029/JA094iA10p13527
386
387 Winick, J. R., R. H. Picard, R. D. Sharma, R. A. Joseph, and P. P. Wintersteiner (1987),
388 Radiative Transfer Effects on Aurora Enhanced 4.3 Micron Emission, Adv. Space Res. Vol. 7,
389 No. 10, 17-21.
390
391 Winick, J. R., M. G. Mlynczak, P. P. Wintersteiner, F. J. Martin-Torres, R. H. Picard, L. J.
392 Paxton, M. Lopez-Puertas, J. M. Russell III, A. B. Christensen, L. L. Gordley (2004),
393 Thermospheric infrared radiance response to the April 2002 geomagnetic storm from SABER
394 infrared and GUVI ultraviolet limb data, Proceedings of the SPIE, Volume 5235,
395 doi:10.1117/12.515982.
396

397

Figure 1.

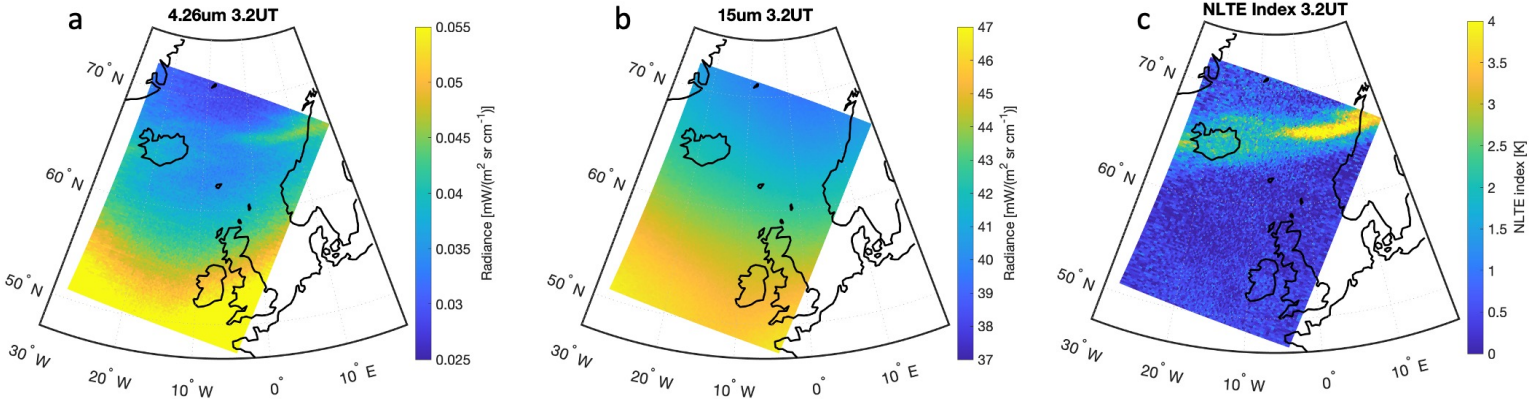
a
4.26um 3.2UT
70˚N
60˚N
50˚N
30˚W
20˚W
10˚W
0˚
10˚E
0.055
0.05
0.045
0.04
0.035
0.03
0.025
Radiance [mW/(m2 sr cm-1)]
b
15um 3.2UT
70˚N
60˚N
50˚N
30˚W
20˚W
10˚W
0˚
10˚E
47
46
45
44
43
42
41
40
39
38
37
Radiance [mW/(m2 sr cm-1)]
c
NLTE Index 3.2UT
70˚N
60˚N
50˚N
30˚W
20˚W
10˚W
0˚
10˚E
4
3.5
3
2.5
2
1.5
1
0.5
0
NLTE index [K]

Figure 2.

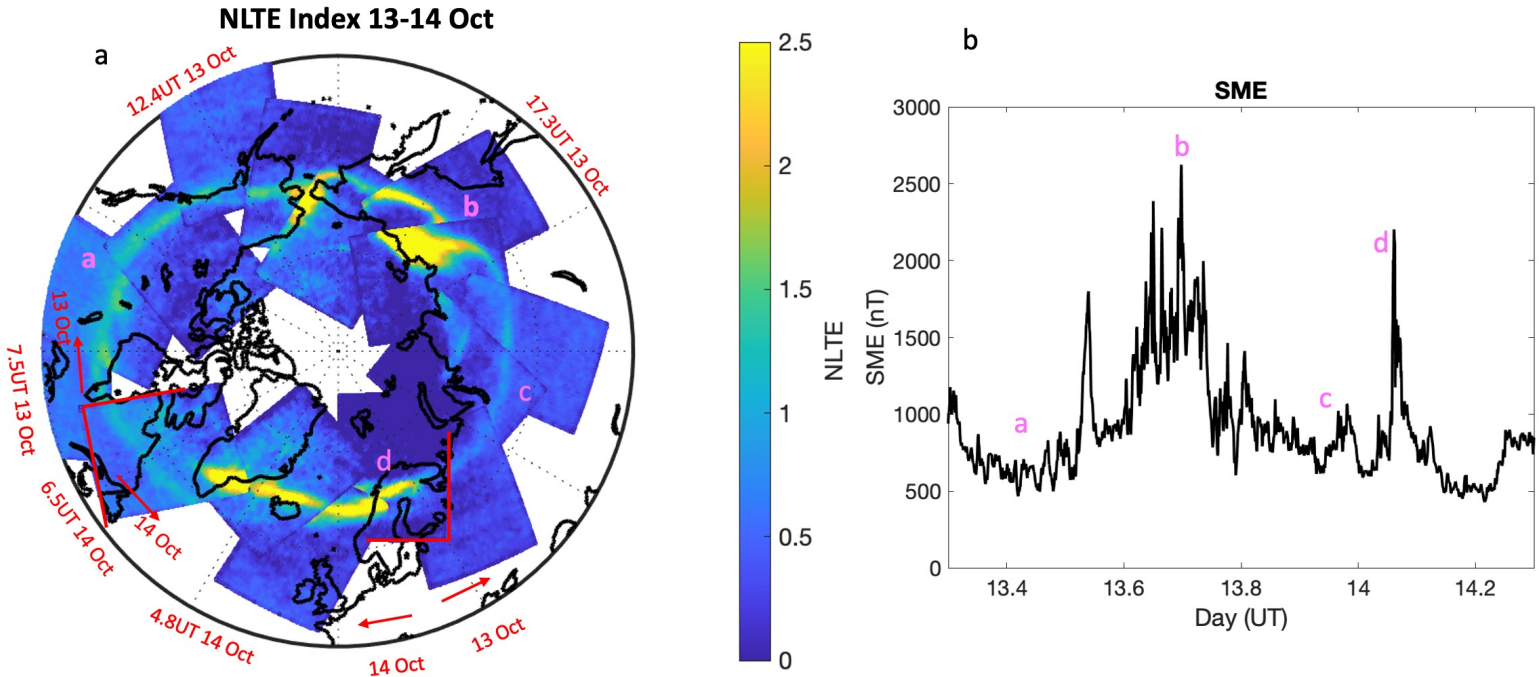
NLTE Index 13-14 Oct
a
12.4UT 13 Oct
17.3UT 13 Oct
7.5UT 13 Oct
13 Oct
6.5UT 14 Oct
14 Oct
4.8UT 14 Oct
14 Oct
13 Oct
a
b
c
d
2.5
2
1.5
1
0.5
0
NLTE
b
SME
3000
2500
2000
1500
1000
500
0
SME (nT)
a
b
c
d
13.4
13.6
13.8
14
14.2
Day (UT)

Figure 3.

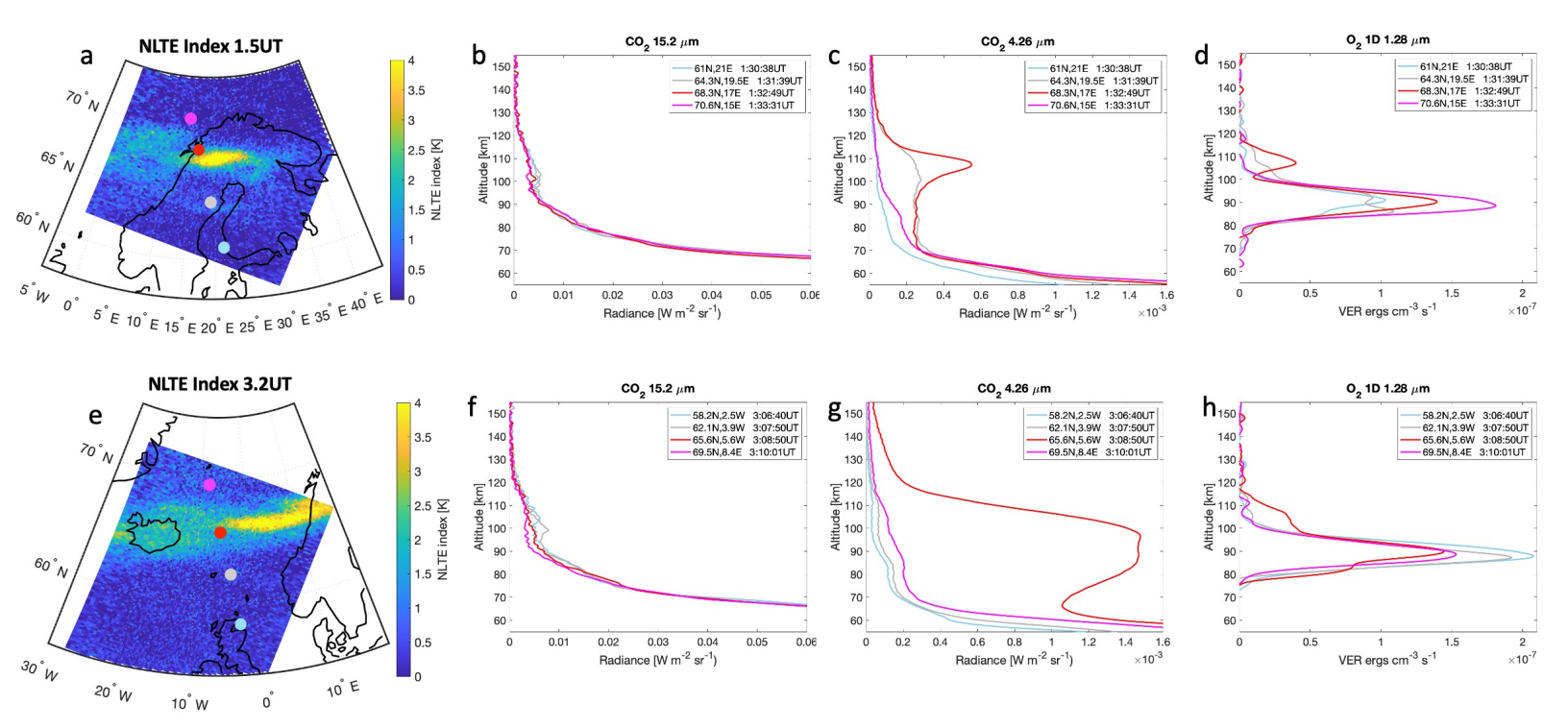
a
NLTE Index 1.5UT
70 ˚N
65 ˚N
60 ˚N
5 ˚W
0 ˚
5 ˚E
10 ˚E
15 ˚E
20 ˚E
25 ˚E
30 ˚E
35 ˚E
40 ˚E
NLTE index [K]
b
CO2 15.2 μm
61N,21E 1:30:38UT
64.3N,19.5E 1:31:39UT
68.3N,17E 1:32:49UT
70.6N,15E 1:33:31UT
Altitude [km]
Radiance [W m-2 sr-1]
c
CO2 4.26 μm
61N,21E 1:30:38UT
64.3N,19.5E 1:31:39UT
68.3N,17E 1:32:49UT
70.6N,15E 1:33:31UT
Altitude [km]
Radiance [W m-2 sr-1]
×10-3
d
O2 1D 1.28 μm
61N,21E 1:30:38UT
64.3N,19.5E 1:31:39UT
68.3N,17E 1:32:49UT
70.6N,15E 1:33:31UT
Altitude [km]
VER ergs cm-3 s-1
×10-7
e
NLTE Index 3.2UT
70 ˚N
60 ˚N
30 ˚W
20 ˚W
10 ˚W
0 ˚
10 ˚E
NLTE index [K]
f
CO2 15.2 μm
58.2N,2.5W 3:06:40UT
62.1N,3.9W 3:07:50UT
65.6N,5.6W 3:08:50UT
69.5N,8.4E 3:10:01UT
Altitude [km]
Radiance [W m-2 sr-1]
g
CO2 4.26 μm
58.2N,2.5W 3:06:40UT
62.1N,3.9W 3:07:50UT
65.6N,5.6W 3:08:50UT
69.5N,8.4E 3:10:01UT
Altitude [km]
Radiance [W m-2 sr-1]
×10-3
h
O2 1D 1.28 μm
58.2N,2.5W 3:06:40UT
62.1N,3.9W 3:07:50UT
65.6N,5.6W 3:08:50UT
69.5N,8.4E 3:10:01UT
Altitude [km]
VER ergs cm-3 s-1
×10-7

Figure 4.

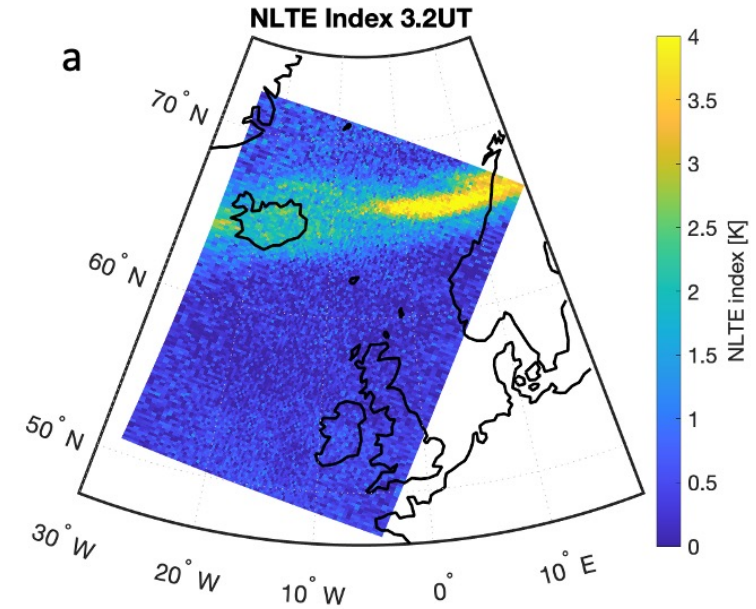
a
NLTE Index 3.2UT
70 ˚ N
60 ˚ N
50 ˚ N
30 ˚ W
20 ˚ W
10 ˚ W
0 ˚
10 ˚ E
NLTE index [K]
0
0.5
1
1.5
2
2.5
3
3.5
4

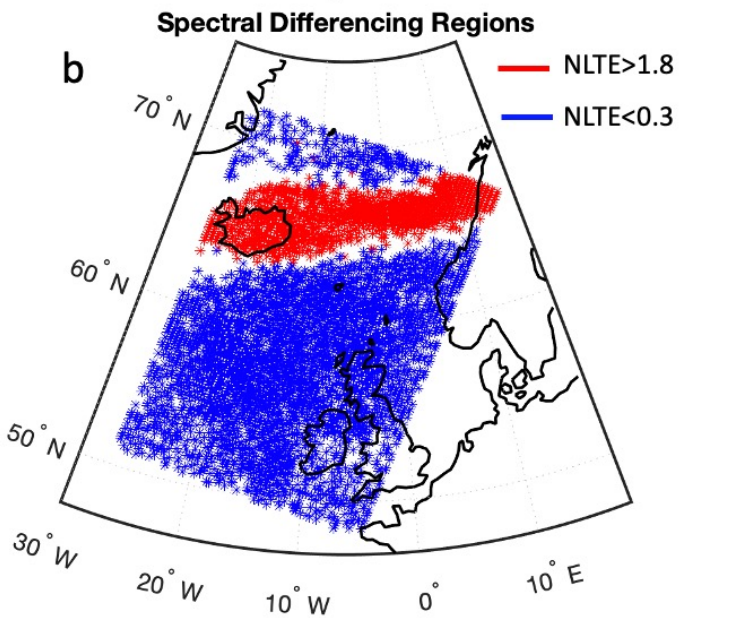
b
Spectral Differencing Regions
NLTE>1.8
NLTE<0.3
70 ˚ N
60 ˚ N
50 ˚ N
30 ˚ W
20 ˚ W
10 ˚ W
0 ˚
10 ˚ E

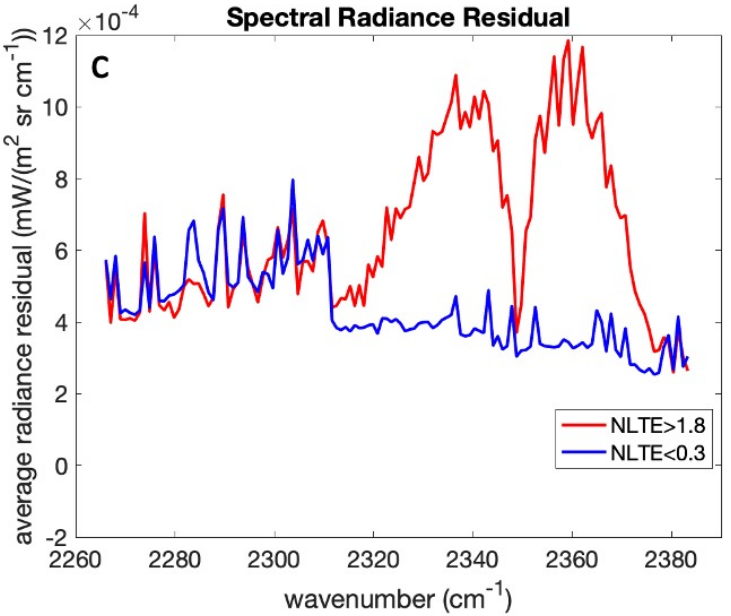
c
Spectral Radiance Residual
×10^-4
average radiance residual (mW/(m^2 sr cm^-1))
wavenumber (cm^-1)
NLTE>1.8
NLTE<0.3
2260
2280
2300
2320
2340
2360
2380

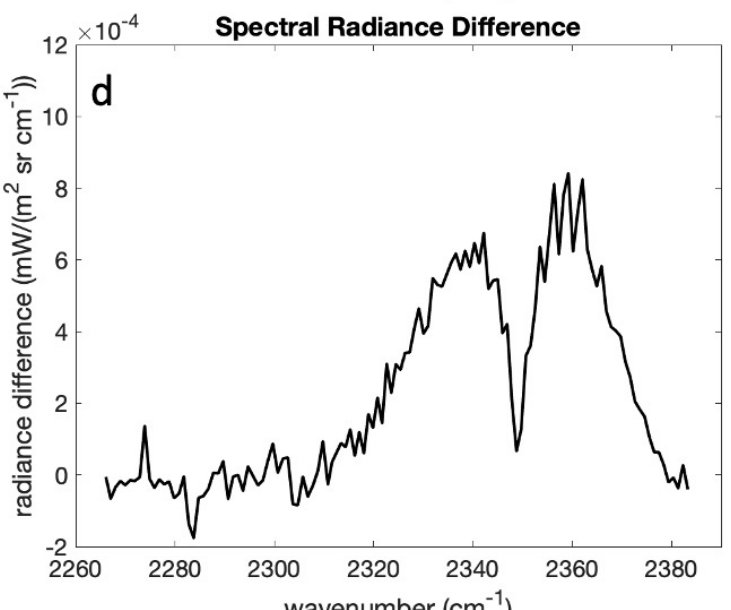
d
Spectral Radiance Difference
×10^-4
radiance difference (mW/(m^2 sr cm^-1))
wavenumber (cm^-1)
2260
2280
2300
2320
2340
2360
2380